

PTEN Knockdown Alters Dendritic Spine/Protrusion Morphology, not Density

Michael E. Haws,^{1,2} Thomas C. Jaramillo,¹ Felipe Espinosa,¹ Allie J. Widman,¹ Garret D. Stuber,⁷ Dennis R. Sparta,⁷ Kay M. Tye,⁷ Scott J. Russo,³ Luis F. Parada,⁴ Mihaela Stavarache,⁵ Michael Kaplitt,⁵ Antonello Bonci,^{6,8} and Craig M. Powell^{1,2,9*}

¹Department of Neurology & Neurotherapeutics, The University of Texas Southwestern Medical Center, Dallas, Texas 75390-8813

²Neuroscience Graduate Program, The University of Texas Southwestern Medical Center, Dallas, Texas 75390-8813

³Department of Neuroscience, Icahn School of Medicine at Mount Sinai, New York, New York 10029

⁴Department of Developmental Biology, The University of Texas Southwestern Medical Center, Dallas, Texas 75390

⁵Department of Neurological Surgery, Weill Cornell Medical College, New York, New York 10065

⁶National Institute on Drug Abuse, Intramural Research Program, Bethesda, Maryland 21224

⁷Department of Neurology, University of California San Francisco, San Francisco, California 94143

⁸Solomon H. Snyder Department of Neuroscience and Department of Psychiatry, Johns Hopkins School of Medicine, Baltimore, Maryland 21287

⁹Department of Psychiatry, The University of Texas Southwestern Medical Center, Dallas, Texas 75390-8813

ABSTRACT

Mutations in phosphatase and tensin homolog deleted on chromosome 10 (PTEN) are implicated in neuropsychiatric disorders including autism. Previous studies report that PTEN knockdown in neurons *in vivo* leads to increased spine density and synaptic activity. To better characterize synaptic changes in neurons lacking PTEN, we examined the effects of shRNA knockdown of PTEN in basolateral amygdala neurons on synaptic spine density and morphology by using fluorescent dye confocal imaging. Contrary to previous studies in the dentate gyrus, we find that knockdown of PTEN in basolateral amygdala leads to a significant decrease in total spine density in distal dendrites. Curiously, this decreased spine density is associated with increased miniature excitatory postsynaptic current frequency and amplitude, suggesting an increase in number and function of mature spines. These seemingly contradictory findings were reconciled by spine morphology analysis demon-

strating increased mushroom spine density and size with correspondingly decreased thin protrusion density at more distal segments. The same analysis of PTEN conditional deletion in the dentate gyrus demonstrated that loss of PTEN does not significantly alter total density of dendritic protrusions in the dentate gyrus, but does decrease thin protrusion density and increases density of more mature mushroom spines. These findings suggest that, contrary to previous reports, PTEN knockdown may not induce *de novo* spinogenesis, but instead may increase synaptic activity by inducing morphological and functional maturation of spines. Furthermore, behavioral analysis of basolateral amygdala PTEN knockdown suggests that these changes limited only to the basolateral amygdala complex may not be sufficient to induce increased anxiety-related behaviors. *J. Comp. Neurol.* 522:1171–1190, 2014.

© 2013 Wiley Periodicals, Inc.

INDEXING TERMS: dendrite; spine; amygdala; dentate gyrus; AKT; mTOR; PTEN

Drs. Stuber and Sparta's present address is Psychiatry, University of North Carolina, Chapel Hill, NC 27599-7250.

Dr. Tye's present address is Department of Brain and Cognitive Sciences, Picower Institute for Learning and Memory, Massachusetts Institute of Technology, Cambridge, MA 02139.

Grant sponsor: National Institute of Mental Health, National Institutes of Health; Grant number: MH081164 (to C.M.P.); Grant sponsor: National Institute of Child Health and Human Development, National Institutes of Health; Grant number: HD069560 (to C.M.P.); Grant sponsor: Autism Speaks (to C.M.P.); Grant sponsor: Lowe Foundation (to C.M.P.); Grant sponsor: Crystal Charity Ball (to C.M.P.); Grant sponsor: The Hartwell Foundation (to C.M.P.).

*CORRESPONDENCE TO: Craig M. Powell, 5323 Harry Hines Blvd., Dallas, TX 75390-8813. E-mail: craig.powell@utsouthwestern.edu

Received May 13, 2013; Revised October 2, 2013; Accepted October 3, 2013.

DOI 10.1002/cne.23488

Published online November 21, 2013 in Wiley Online Library (wileyonlinelibrary.com)

© 2013 Wiley Periodicals, Inc.

Phosphatase and tensin homolog deleted on chromosome ten (PTEN) is a lipid and protein phosphatase that negatively regulates the phosphatidylinositol 3-kinase (PI3K)/AKT/mTOR signaling pathway, ultimately modulating cell growth and protein translation (Besson et al., 1999; Dahia, 2000; Di Cristofano and Pandolfi, 2000; Downes et al., 2001; Eng, 1999, 2003; Hobert and Eng, 2009; Hoeffler and Klann, 2010; Leslie and Downes, 2002; Maehama and Dixon, 1998, 1999; Orloff and Eng, 2008; Vazquez and Sellers, 2000; Waite and Eng, 2002). *PTEN* was originally discovered as the gene responsible for a subset of familial hamartoma syndromes associated with increased risk for certain cancers (Nelen et al., 1997) and as a gene often mutated in human cancers and tumor cell lines (Li et al., 1997; Steck et al., 1997). More recently, mutations in *PTEN* have been linked directly to autism with macrocephaly and neurodevelopmental delay with macrocephaly, findings that have been replicated by multiple laboratories in multiple cohorts (Boccone et al., 2006; Butler et al., 2005; Buxbaum et al., 2007; Goffin et al., 2001; Herman et al., 2007; McBride et al., 2010; Orrico et al., 2009; Stein et al., 2010; Varga et al., 2009; Zori et al., 1998). Thus, understanding *PTEN*'s role in neuronal morphology and function is important for understanding human neuropsychiatric disease.

PTEN deficiency results in erratic neuronal migration, neuronal hypertrophy, and abnormal arborization and myelination in humans (Abel et al., 2005) and in animal models (Backman et al., 2001; Fraser et al., 2008; Kwon et al., 2001, 2006; Xiong et al., 2012). By using Golgi staining or immunohistochemistry, we and others have demonstrated that *PTEN*-deficient neurons in brains of animal models have increased synaptic spine density (Fraser et al., 2008; Kwon et al., 2006; Luikart et al., 2011; Pun et al., 2012; Zhou et al., 2009) and increased frequency of miniature excitatory postsynaptic currents (mEPSCs) (Luikart et al., 2011), whereas *PTEN* overexpression can decrease apparent synaptic spine density (Zhang et al., 2012), findings suggestive of a role for *PTEN* in de novo synapse and synaptic spine formation.

Using sensitive fluorescent dye measures (Dumitriu et al., 2010, 2011, 2012a,b), we have performed a detailed analysis of synaptic spine/dendritic protrusion density and morphology in two different populations of central neurons with shRNA knockdown or transgenic deletion of *PTEN*. Interestingly, with these methods we do not find an increased dendritic protrusion density, but rather an overall *decrease* in total dendritic protrusion density in the basolateral amygdala complex (BLA; comprised of the basolateral and lateral nuclei of the amygdala) neurons associated with a *decrease* in den-

sity of thin protrusions at distal dendritic segments and an *increase* in density of more "mature," mushroom-shaped spines all along the dendritic tree. In the dentate gyrus (DG) granule neurons we find no change in overall dendritic protrusion density, but the same shift in protrusion morphology: decreased thin protrusions and increased mushroom spines. Head diameter of mushroom-shaped spines is also significantly increased. These changes are accompanied by increased frequency and amplitude of mEPSCs onto *PTEN*-deficient neurons, implying that this structural spine maturation is accompanied by concomitant functional maturation. These results implicate *PTEN* and the PI3K/AKT/mTOR pathway in functional and structural alterations in dendritic protrusions rather than de novo spine formation. Finally, although we cannot completely rule out a role for *PTEN* in the BLA in anxiety-related behaviors, our data suggest that focal, limited *PTEN* knockdown and the correlated increased mushroom spine density in the BLA is not sufficient to cause anxiety-like behavioral phenotypes that have previously been correlated with increased BLA spine density and anxiety-like behaviors following chronic stress (Lakshminarasimhan and Chattarji, 2012).

MATERIALS AND METHODS

Recombinant adeno-associated virus

Viruses were constructed and purified by the laboratory of Dr. Michael Kaplitt (Weill Cornell Medical College, New York, NY). Recombinant adeno-associated virus (rAAV) vectors encoding for luciferase-silencing or *PTEN*-silencing short hairpin loop RNA (shLuciferase [shLuc] and sh*PTEN*, respectively) sequences were generated as follows: DNA oligos encoding shLuc and sh*PTEN* were annealed and cloned immediately downstream from the human PolIII H1 promoter into *Bgl*II and *Xba*I sites of an rAAV vector. The following oligos were used: 5'-GATCCCCCGCTGGAGAGCAACTGCATTTCAAGAGA ATGCAGTTGCTCTCCAGCGGTTTTGGAA-3' (shLuc) and 5'-GATCCCCGAGTTCTCCACAAACAGAACTCCTGTCA TTCTGTTTGTGAAGAAGCTTTTTTGAAT-3' (sh*PTEN*). The underlined regions are the target-specific sequences separated by the loop sequence. The rAAV vector bicistronically expresses yellow fluorescent protein (YFP) under the control of the hybrid cytomegalovirus (CMV) enhancer/chicken β -actin promoter. Vector stocks were prepared by packaging the plasmids into AAV serotype 2 particles by using a helper-free plasmid transfection system. Serotype 2 has been shown to have specificity for neurons over microglia and astrocytes (Bartlett et al., 1998). The vectors were purified using heparin affinity chromatography and dialyzed

TABLE 1.
Primary Antibodies Used in This Study

Antibody	Type	Host	Immunogen	Dilution	Source	Cat. no.	JCN antibody Registry ID
Anti-GFP	Polyclonal	Rabbit	Purified GFP from jellyfish <i>Aequorea Victoria</i>	1:2,000	Invitrogen	A6455	AB_22150
Anti-GFP	Polyclonal	Chicken	Purified Recombinant GFP	1:2,000	Aves Labs	1020	AB_10000240
Anti-NeuN	Monoclonal	Mouse	Purified cell nuclei from mouse brain	1:250	Chemicon	MAB377	AB_2298772
Anti-PTEN	Monoclonal	Rabbit	Epitope surrounds amino acid 395 of PTEN sequence	1:400	Cell Signaling	9188	AB_2174349
Anti-pAKT	Monoclonal	Rabbit	Epitope surrounds serine 473 of AKT sequence	1:200	Cell Signaling	4060	AB_916027

Abbreviations: JCN, Journal of Comparative Neurology; GFP, green fluorescent protein; NeuN, neuronal nuclei; PTEN, phosphate and tensin homolog; pAKT, phosphorylated AKT.

against phosphate-buffered saline (PBS). AAV titers were determined quantitative polymerase chain reaction (PCR) using CMV enhancer-specific primers and adjusted to 10^{11} genomic particles per ml. The integrity and accuracy of all constructs were verified by sequencing.

Intracranial viral injections

Seven-week-old male C57BL/6J mice were anesthetized with 0.1 ml of a 20% ketamine, 10% xylazine in 0.9% saline solution, mounted onto a mouse stereotaxic apparatus (Kopf Instruments, Tujunga, CA), and sterilized with ethanol and povidone-iodine (Betadine, Purdue, Stamford, CT). Holes in the skull were drilled 1.2 mm posterior, 3.25 mm lateral to bregma bilaterally, and a pulled glass capillary pipette (Sutter Instruments, Novato, CA) containing the virus was brought to the brain surface. The pipette was lowered 4.5 mm and 0.5 μ l of AAV-shPTEN or AAV-shLuc was slowly injected into the region of the BLA. Following injections, silk sutures were used to close the wound. The location and spread of viral infection was examined post mortem by using immunohistochemistry (IHC; method described below) to detect YFP expression. Only mice that bilaterally expressed YFP in the BLA without significant YFP expression in the cortex, striatum, or central amygdala were defined as bilateral BLA hits and used for experimental analysis. This determination took place after the experiments were completed by an investigator blind to the experimental results of each individual mouse. On a randomly chosen, representative subset of the same mice that had undergone viral injections and behavioral testing, we used IHC on 30- μ m-thick brain sections to colocalize the neuronal marker NeuN with virally expressed YFP, and then took high-magnification images within an infected region of the BLA. The percentage of neurons infected was then calculated as the percent of NeuN+ cells that were also YFP+. Three animals were used, from which five slices were ana-

lyzed from each mouse and averaged together. Immunohistochemical, electrophysiological, and morphological experiments were performed 3 weeks after surgeries. All experiments were done in accordance with National Institutes of Health and University of Texas Southwestern Medical Center animal guidelines and protocols.

Immunohistochemistry

Virus-injected mice were perfused with 4% paraformaldehyde (PFA; Sigma, St. Louis, MO), and then whole brains were postfixed in 4% PFA at 4°C overnight. Brains were transferred to 30% sucrose (Sigma) and allowed to equilibrate until they sank. Then 30- μ m sections were cut (HM 430 Sliding microtome, Microm, Waldorf, Germany) at dry ice temperatures and stored at 4°C in PBS containing 0.1% sodium azide (Sigma) until use. Tissue sections were mounted onto positively charged glass slides (Fisher, Waltham, MA) and allowed to air dry. A 0.1 M citric acid (Sigma) antigen unmasking treatment was performed prior to blocking slices with 3% normal donkey serum (NDS; Jackson ImmunoResearch, West Grove, PA) in PBS containing 0.3% Triton X-100 (Sigma). Overnight primary antibody incubation in 3% NDS, 0.3% Tween-20 (Sigma) in PBS at room temperature was followed by a 2-hour secondary antibody treatment. Tyramide amplification was performed using the Avidin Biotin Complex Kit (Vector, Burlingame, CA) and a Tyramide Signal Amplification Kit (PerkinElmer, Waltham, MA). Images were taken on an Olympus BX51 epifluorescent microscope (Tokyo, Japan).

Antibody characterization

Primary antibody details, sources, and their concentrations are shown in Table 1. Secondary antibodies used were fluorescein isothiocyanate (FITC)-conjugated donkey anti-chicken, FITC-conjugated donkey anti-rabbit, CY3-conjugated donkey anti-mouse, and biotin-

conjugated donkey anti-rabbit (Jackson ImmunoResearch).

The rabbit anti-green fluorescent protein (GFP) antibody (Invitrogen, Carlsbad, CA) recognizes the gene product of GFP-expressing transgenic mice and is not reactive with non-GFP-expressing mice (Moldrich et al., 2010). In the current study, staining was only observed in brain regions infected with either shPTEN or shLuc, which express the *Aequorea victoria* fluorescent protein color variant YFP.

The chicken anti-GFP antibody (Aves Labs, Tigard, OR) recognizes the gene product of GFP-expressing transgenic mice and is not reactive with non-GFP-expressing mice (Encinas et al., 2006); the specificity has been verified by the manufacturer with western blot. In the current study, staining was only observed in brain regions infected with either shPTEN or shLuc, which express the *Aequorea victoria* fluorescent protein color variant YFP.

The mouse anti-NeuN (Millipore, Billerica, MA) antibody recognizes the DNA-binding neuron-specific protein NeuN, which is present in most neuronal cell types of vertebrate central nervous system (CNS). It does not stain non-neuronal cell types. It stains only nuclei in a neuronal pattern consistent with previous findings in the mouse brain (Mullen et al., 1992).

The rabbit anti-PTEN antibody (Cell Signaling Technology, Danvers, MA) recognizes PTEN protein. Specificity of this antibody was shown by western blot by using whole cell lysates of the endometrial cancer cell line Hec-1b with wild-type PTEN and of the breast cancer cell line MDA-MB-415 harboring a PTEN mutation. No PTEN immunoreactivity was observed in the mutant line by western blot (Forster et al., 2011). The specificity has also been verified by the manufacturer with western blot by using HeLa, COS-7, and C6 cell lines.

The rabbit anti-pAKT antibody (Cell Signaling Technology) recognizes the akt protein when phosphorylated at serine 473. Specificity for phosphorylated Akt was shown by the manufacturer by western blot. When PC-3 cells were pretreated with LY249002 and Wortmanin, the immunoreactive band at ~62 kDa is absent, whereas the antibody is immunoreactive with untreated PC-3 cells.

Neuronal morphology and dendritic protrusion density

Basolateral amygdala neurons

Mouse brain tissue was prepared for intracellular loading of neurons in the BLA with Alexa Fluor 568 following methods reported by Dumitriu et al. (2010, 2011), with minor modifications. Mice used for dendritic pro-

trusion analysis were injected with virus and then sacrificed between 21 and 25 days later. Mouse injections were staggered so that we could sacrifice two mice at a time (one shLuc and one shPTEN), allowing for perfusion, cell filling, and confocal imaging to be done within 72 hours. Virus-injected mice were perfused with 5 ml of 1% PFA in 0.1 M phosphate buffer, pH 7.4 (PB) followed by 60 ml of 4% PFA and 0.125% glutaraldehyde in 0.1 M PB at 5 ml/min. Brains were postfixed for 2 hours in 4% PFA and 0.125% glutaraldehyde in 0.1 M PB, and then 225- μ m-thick slices were cut on a Vibratome in chilled 1X PBS (Fisher, Waltham, MA) and stored in 1X PBS at 4°C until use.

Loading of virally infected neurons with Alexa Fluor 568 (Invitrogen) was performed as previously described (Hao et al., 2006) with minor modifications. Sections were immersed in 1X PBS, and virally infected neurons of the BLA were identified by epifluorescence, impaled with sharp micropipettes, and loaded with 10 mM Alexa Fluor 568 in 200 mM KCl under a direct current of 1–4 nA for 5–10 minutes, or until the dye filled distal processes and no additional loading was observed. Per mouse, 5–10 neurons were loaded with dye, and two to four neurons were loaded per slice. Sections containing loaded cells were mounted on glass slides, and covered with H-1000 Vectashield mounting medium (Vector). Confocal z-stacks of filled neurons contained 50–80 images 2 μ m apart and were captured with a Plan-Achromat 20 \times /0.75 NA objective lens on a Zeiss (Peabody, MA) Laser Scanning Microscope (LSM) 510. Filled neurons had to meet four criteria to be kept for morphological and dendritic protrusion analysis:

1. The neuron had to be located in the BLA.
2. The neuron had to express YFP, detected with 3D imaging taken by confocal fluorescent microscopy (LSM 510, Zeiss).
3. Due to differences in morphology and dendritic protrusion density between different neuron types in the BLA, the neuron had to be a class I neuron (McDonald, 1982). Class I neurons were defined as cells with a soma at least 15 μ m in diameter, at least five primary dendrites, and at least three quaternary branches derived from different primary branches.
4. The center of the cell body had to be located 20–35 μ m beneath the surface of the slice so that a consistent portion of the total dendritic arbor would be included in the morphological analysis.

3D digital reconstructions of neurons were created by using NeuroLucida, and morphological analysis was performed with NeuroExplorer (MBF Bioscience, Williston, VT). After excluding cells that did not meet these criteria, 17 shLuc-infected cells from five mice and 16

shPTEN-infected cells from five mice were included in the amygdala study.

Printouts of neuronal reconstructions that included a series of scaled, concentric circles 10 μm apart centered on the cell body were used to pseudo-randomly select dendritic segments for spine/protrusion analysis. We selected one dendritic segment every 10 μm from the cell body up to 100 μm . Confocal z-stacks of dendritic segments containing up to 60 images 0.2 μm apart were captured with a 100 \times /1.4 NA oil immersion objective lens on a Zeiss LSM 510. Dendritic segments had to meet three criteria to be imaged and included in analysis: 1) the dendritic segment had to span a 10- μm thick circular band created by two adjacent concentric circles; 2) the dendritic segment had to be nearly parallel to the surface of the slice, such that the entire segment could be imaged within a 6- μm -thick z-stack; and 3) no branching or crossing of nearby labeled dendrites could be observed within the segment.

Settings for pinhole size, aperture gain, and offset were optimized initially and then held constant throughout the study to ensure that all images were digitized under the same illumination conditions at a resolution of 0.032 $\mu\text{m} \times 0.032 \mu\text{m} \times 0.2 \mu\text{m}$ per voxel. One high-magnification image was taken every 10 μm from the soma up to 100 μm from the soma. The confocal z-stacks were deconvolved with AutoDeblur (Media Cybernetics, Bethesda, MD) and imported into NeuronStudio (available for download online at <http://research.mssm.edu/cnic/tools-ns.html>, Icahn School of Medicine at Mount Sinai, New York, NY) for semiautomated 3D dendrite segment width and length, spine/protrusion density, spine/protrusion head diameter, and spine classification analysis as previously reported (Rodriguez et al., 2006, 2008; Wearne et al., 2005). Briefly, the spine/protrusion density was calculated by dividing the total number of protrusions present by the length of the dendritic segment. Spine/protrusion subtypes were characterized by using NeuronStudio as follows: A protrusion was deemed stubby if no neck was identified and the total length of the protrusion was $< 2.5 \times$ the width of the base of the protrusion. A protrusion was classified as a thin protrusion when no neck was identified but its total length was $> 2.5 \times$ the width of the identified base of the spine, or when a neck was identified but the head diameter was $< 0.37 \mu\text{m}$. A mushroom spine was classified as a spine with a neck and a head diameter $> 0.37 \mu\text{m}$.

Details regarding the algorithms used to calculate head diameter and neck length have been published elsewhere (Rodriguez et al., 2008). Of note, head diameter is taken as the largest diameter of the head in 3D space. The head diameter threshold of 0.37 μm was

obtained by manually classifying spines in a subset of shLuc neurons and plotting the head diameter distribution of thin and mushrooms protrusions. The intersection of those distributions was used as the head diameter threshold. No distinction was made between filopodia and thin spines, and thus both are included in the thin protrusion category due to difficulties in resolving the difference at the light microscope level. A Student's *t*-test was used for statistical analysis except when distance was included as a repeated measure factor, in which case a two-way analysis of variance (ANOVA) with repeated measures was used.

Dentate gyrus granule neurons

PTEN^{loxP} mice (Suzuki et al., 2001) and Nse-cre mice (Kwon et al., 2006) were provided by Dr. Luis Parada and have been characterized in previous reports. Briefly, both lines have been maintained on a C57BL/6 inbred background. PTEN mutant mice (Nse-cre;PTEN^{loxP/loxP}) were generated by breeding male PTEN^{loxP/loxP} mice and female Nse-cre;PTEN^{loxP/+} mice. Controls used here were PTEN^{loxP/loxP} littermates without cre. Mice were sacrificed for spine/protrusion analysis at 6 months of age. Tissue was prepared in the same manner as above, with the exception that prior to cell filling, slices were stained with 4,6-diamidino-2-phenylindole (DAPI) so that the DG cell body layer could be identified. Cells were filled in the same manner as stated above, except that DG cell body layer neurons were chosen at random. Whole cell morphological analysis was not performed, but dendritic segments of filled cells were selected for confocal imaging based on three criteria:

1. The dendritic segment had to span the 20–50- μm distance from the edge of the cell body layer.
2. The dendritic segment had to be nearly parallel to the surface of the slice, such that the entire segment could be imaged within a 6- μm -thick z-stack.
3. No branching or crossing of nearby dendrites could be observed within the segment.

Dendrite width, spine/protrusion density, and spine/protrusion head diameter were all analyzed as stated above except that manual classification of spines/protrusions from a subset of the WT DG granule neurons provided a head diameter threshold of 0.5 μm .

Electrophysiology

Spontaneous, miniature synaptic transmission in amygdala

Coronal slices (300 μm thick) including the BLA were prepared, and recordings were performed as described previously (Stuber et al., 2011). Briefly, 3–5 weeks after

stereotaxic injections of the viral vectors (see above), mice were anesthetized with pentobarbital, perfused intracardially with 20–30 ml of modified 0°C artificial cerebrospinal fluid (aCSF), and decapitated. The brain was quickly isolated and chilled into dissecting solution. The dissecting solution contained the following (in mM): 75 sucrose, 81 NaCl, 2.5 KCl, 1.0 NaH₂PO₄, 0.1 CaCl₂, 4.9 MgCl₂, 26.2 NaHCO₃, and 1.5 glucose (300–305 mOsm). The bathing solution contained the following (in mM): 119 NaCl, 2.5 KCl, 1.25 NaH₂PO₄, 2.5 CaCl₂, 1 MgCl₂, 26.2 NaHCO₃, and 10 dextrose, saturated with 95% O₂/5% CO₂. For recording of mEPSCs, the bathing solution was supplemented with tetrodotoxin (0.5 μM) and picrotoxin (100 μM).

Slices were incubated in the bathing solution at 32°C for at least 1 hour. Afterward, slices were kept at 32°C or room temperature until they were transferred to a submersion-type recording chamber. Whole-cell patch-clamp recordings from BLA neurons clearly identifiable as expressing YFP from the control or experimental viruses were performed by using micropipettes (3–5 MΩ) made from 1.1/1.5 mm borosilicate glass (Sutter, Novato, CA or King Precision Glass, Claremont, CA). Recording pipettes were filled with the following solution (in mM): 117 Cs-methanesulphonate, 2.8 NaCl, 5 tetraethylammonium (TEA)-Cl, 0.4 ethylene glycol tetraacetic acid (EGTA), 2 adenosine triphosphate (ATP)-Mg, 0.25 guanosine triphosphate (GTP)-Mg, 20 hydroxyethylpiperazine ethanesulfonic acid (HEPES)-CsOH (pH 7.2–7.4, 275–285 mOsm). Access resistance was frequently checked to be <25 MΩ and stable (less than 20% of variability). Recordings were obtained by using the 700B Multiclamp amplifier (Molecular Devices, Palo Alto, CA), and neurons were visualized by using a fluorescent microscope equipped with infrared differential interference contrast. All responses were digitized at 10 kHz and filtered at 1 kHz. Data were analyzed offline using pClamp, MiniAnalysis (Synaptosoft, Fort Lee, NJ), and Microsoft Excel. Student's *t*-test was used to evaluate the significance of all analyses.

Behavior

Behaviors were done on two cohorts of mice with less stressful tests at the beginning and more stressful tests toward the end in the following order: elevated plus maze, dark/light, open field, locomotor, social interaction with a juvenile, social interaction in an open field, startle threshold, contextual and cued fear conditioning, and footshock threshold (McIlwain et al., 2001). The behavioral tests were begun at 3 weeks post virus injection. Mice were given a 24-hour intertest interval throughout the test battery (Paylor et al., 2006). Mice were allowed 1 hour to habituate to the testing room

prior to beginning experiments. Significance was taken as $P < 0.05$ for all behaviors. Only mice with clear, bilateral BLA viral targeting were included in the study ($n = 15$ AAV-PTEN-shRNA injected mice and $n = 12$ AAV-Luciferase-shRNA injected mice). All tests were done in accordance with IACUC and University of Texas Southwestern Medical Center animal guidelines and protocols.

Tests of anxiety

Tests of anxiety were performed as previously reported (Tabuchi et al., 2007). For the *elevated plus maze* task, mice were placed in the center of a black plexiglass elevated plus maze (each arm 33 cm in length and 5 cm wide, with 25-cm-high walls on closed arms) in a dimly lit room for 5 minutes. Two mazes were used and video-tracked simultaneously (Ethovision 2.3.19, Noldus, Wageningen, The Netherlands). A barrier was set between the mazes to prevent mice from seeing each other. Time spent in open and closed arms, number of open and closed entries, and time in the middle were calculated. Data were analyzed with a one-way ANOVA. The *open field* test was performed for 10 minutes in a brightly lit, 48 × 48 × 48-cm white plastic arena using the Ethovision video-tracking software (Noldus). Time spent in the center zone (15 × 15 cm) and frequency to enter the center were recorded. Locomotor activity was also measured during the open field test. Data were analyzed with a one-way ANOVA. The *dark/light* apparatus is a two-compartment opaque plexiglass box. One side is black and kept closed and dark, whereas the other is white with a fluorescent light directly above its open top. Mice were placed in the dark side for 2 minutes, and then the divider between the two sides was removed, allowing the mouse to freely explore both chambers for 10 minutes. Time spent in the light and in the dark compartments was measured. Measures were taken by using photobeams and MedPC software (Med Associates, St. Albans, VT). Data were analyzed with a one-way ANOVA.

Locomotor

The locomotor test was performed as previously reported (Tabuchi et al., 2007). Mice were placed in a fresh home cage with minimal bedding for a 2-hour testing period. Lengthwise horizontal activity was monitored by using photobeams linked to computer data acquisition software (San Diego Instruments, San Diego, CA). Data were analyzed with a two-way ANOVA with repeated measures (two-way rmANOVA).

Social interaction tests

Tests of social interaction were performed as previously reported (Tabuchi et al., 2007). Direct *social interaction*

with a juvenile took place in a novel, empty, clear, plastic mouse cage under red light as previously reported. Following a 15-minute habituation in the dark, the experimental and target mice were placed in the neutral cage for 2 minutes and allowed to directly interact. Time spent interacting with the juvenile was scored by an observer blind to genotype. Social learning was assessed 3 days later by allowing mice to interact with the same juvenile for an additional 2 minutes. Again, time spent interacting with the juvenile was scored. Data were analyzed with a three-way mixed ANOVA with genotype and sex as between-subjects factors and test session as a within-subjects factor. *Social interaction in the open field* was tested by placing experimental mice in a $48 \times 48 \text{ cm}^2$ white plastic arena by using a $6.0 \times 9.5\text{-cm}$ porous rectangular plexiglass cage with or without an adult mouse as a target, allowing olfactory and minimal tactile interaction. Social interaction was measured as the time spent in the interaction zone (area immediately surrounding the target cage). One-way ANOVA was used to compare time spent in the interaction zones between groups.

Startle threshold

This task was performed exactly as described previously (Blundell et al., 2010). Briefly, mice were presented with six trial types of varying intensity (No Stimulus or 80-, 90-, 100-, 110-, or 120-dB pulses—eight presentations of each). Mean startle amplitudes for each condition were averaged. Data were analyzed with a two-way rmANOVA.

Fear conditioning

Fear conditioning was performed as described previously (Powell et al., 2004). Mice were placed in clear plexiglass shock boxes (Med Associates) for 2 minutes, and then two 90-dB acoustic conditioned stimuli (CS; white noise, each 30 seconds in duration and separated by a 30-second delay) were played. Each CS coterminated in a 2-second, 0.5-mA foot shock (US). Mice remained in the chamber for 2 minutes after the second pairing before returning to their home cages. Freezing behavior (motionless except respirations) was monitored at 5-second intervals by an observer blind to the genotype. To test contextual learning 24 hours later, mice were returned to the same training context and scored for freezing in the same manner. To assess cue-dependent fear conditioning, mice were placed in a novel environment with an unfamiliar vanilla odor in the afternoon following the contextual test. Freezing was measured first during a 3-minute baseline period and then during 3 minutes with the CS playing. Cue-dependent fear conditioning was measured by subtract-

ing the 3-minute baseline period from the 3-minute CS period. Data were analyzed with a one-way ANOVA.

Footshock threshold

Footshock threshold analysis was performed as described previously (Blundell et al., 2009). Briefly, mice were placed in the fear conditioning apparatus for a 2-minute habituation followed by a 2-second footshock with an interstimulus interval of 20 seconds of gradually increasing intensity from 0.05 mA in 0.05-mA steps. The intensity required to elicit flinching, jumping, and vocalizing was recorded by an observer blind to genotype. Data were analyzed with a one-way ANOVA.

RESULTS

Previous studies of Chattarji and colleagues (Govindarajan et al., 2006; Lakshminarasimhan and Chattarji, 2012) demonstrated that following chronic and acute immobilization stress, brain-derived neurotrophic factor (BDNF; an upstream regulator of the PI3K/AKT/mTOR pathway) and spine density concomitantly increase in the basolateral amygdala (BLA) (Lakshminarasimhan and Chattarji, 2012). Furthermore, in BDNF-overexpressing transgenic mice, increased BDNF and increased neuronal spine density in the BLA correlated with increased anxiety (Govindarajan et al., 2006). We initially hypothesized that increased activity of the PI3K/AKT/mTOR pathway via knockdown of PTEN would be sufficient to increase spine density in the BLA. To test this hypothesis, we injected shRNA-expressing AAV serotype 2 into the BLA that would target and knock down PTEN transcripts preferentially in neurons (Bartlett et al., 1998). We then measured neuronal and spine/dendritic protrusion morphology and size.

Characterization of viral injections

In order to knock down PTEN, we used AAV-PTEN-shRNA (shPTEN) injections into the BLA compared with control virus AAV-luciferase-shRNA (shLuc). Because both the shPTEN and shLuc viruses bicistronically expressed YFP, we used IHC against YFP to examine the accuracy of our bilateral viral injections into the BLA 3 weeks after injection (Fig. 1A). We found that more than half of the injected mice showed YFP expression largely contained to the BLA bilaterally. A Paxinos plate overlaid with the localization of viral YFP expression from all the included shPTEN mice is shown in Figure 1B. Mice that did not exhibit YFP expression in the BLA, or that exhibited significant YFP expression in the central amygdala, cortex, or striatum were excluded from our studies in a manner completely blind to other

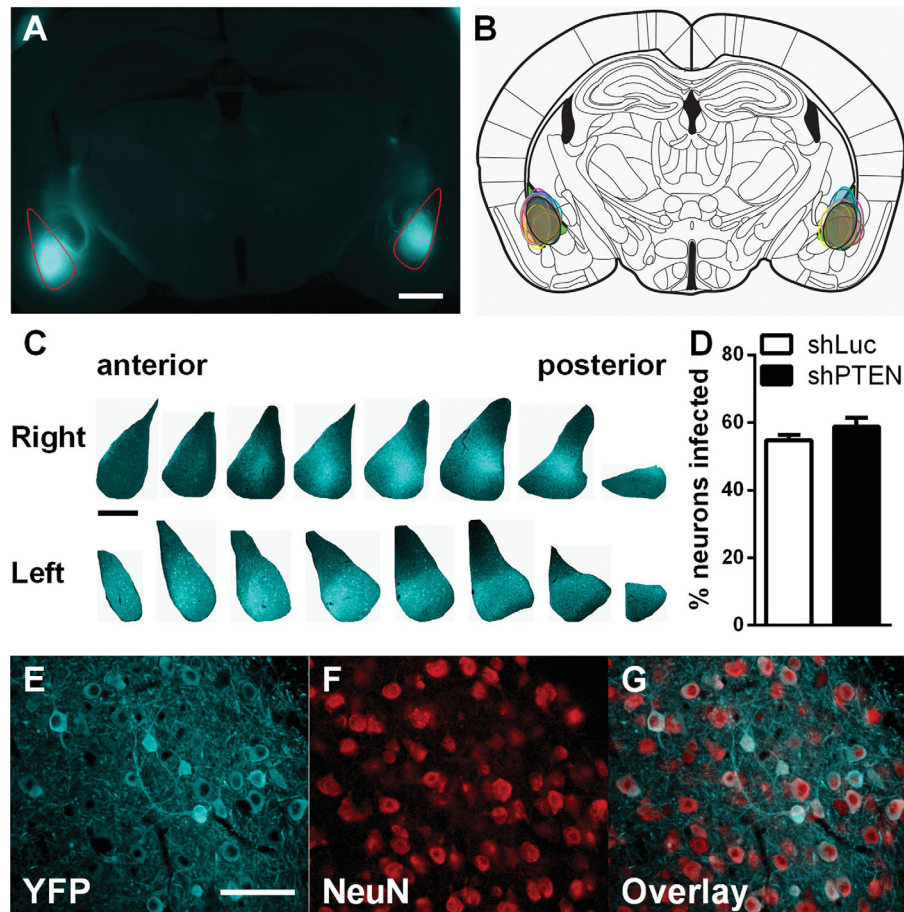


Figure 1. shPTEN and shLuc virus injections target the basolateral amygdala complex. **A:** Example image of bilateral infection of the BLA (outlined in red). **B:** Schematic of a coronal mouse brain section at -1.70 mm relative to bregma (adapted from Paxinos and Franklin, 2001). The BLA is shaded in with bright green. Each oval color represents the viral spread within a single shLuc mouse that was used in behavioral experiments. **C:** Sections of virally infected BLA (sections separated by $180\ \mu\text{m}$) showing anterior-posterior spread of virus. **D:** Quantification of cell counts reported as the percentage of NeuN+ cells that were also YFP+. No difference between groups was observed using Student's *t*-test. $n = 3$ mice for both shPTEN and shLuc groups. **E-G:** Representative images of immunofluorescent staining of YFP (cyan) and NeuN (red). Images were taken within a virally infected region of the BLA, and the numbers of NeuN+ and YFP+ cells were counted. Scale bar = $1\ \text{mm}$ in A; $500\ \mu\text{m}$ in C; $60\ \mu\text{m}$ in E (applies to E-G).

results. To examine the anterior-posterior spread of the virus within the BLA, we again used anti-YFP antibodies to label brain sections taken every $180\ \mu\text{m}$ along the anterior-posterior axis of the amygdala (Fig. 1C). We found that YFP expression spread more than $1\ \text{mm}$ along the anterior-posterior axis.

Finally, we quantified the percentage of neurons expressing YFP within an infected region by colabeling sections with anti-YFP and anti-NeuN antibodies and then calculating the percentage of NeuN+ cells that were also YFP+ (Fig. 1D-G). The percentage of neurons infected by the shPTEN and shLuc viruses was not significantly different (shPTEN, mean \pm standard error of the mean [SEM] $58.80 \pm 1.58\%$; shLuc, $54.81 \pm 1.58\%$; $P = 0.23$, $n = 3$ randomly chosen mice from behavioral

experiments, with data from five slices per mouse averaged together for each of the three mice). Whereas around half of the NeuN+ cells were also YFP+, it is important to note that few of the YFP+ cells were NeuN- (Fig. 1G). Even though small numbers of other cell types may have been infected, labeling for NeuN supports what is already known about the relative neuronal tropism of AAV serotype 2 viruses (Bartlett et al., 1998).

We next tested whether the shPTEN virus effectively resulted in decreased PTEN protein levels by double-labeling YFP and PTEN in brain sections from shPTEN- and shLuc-injected mice. In low-magnification images, shPTEN-infected tissue (Fig. 2A-C) revealed that PTEN protein levels were significantly decreased in regions

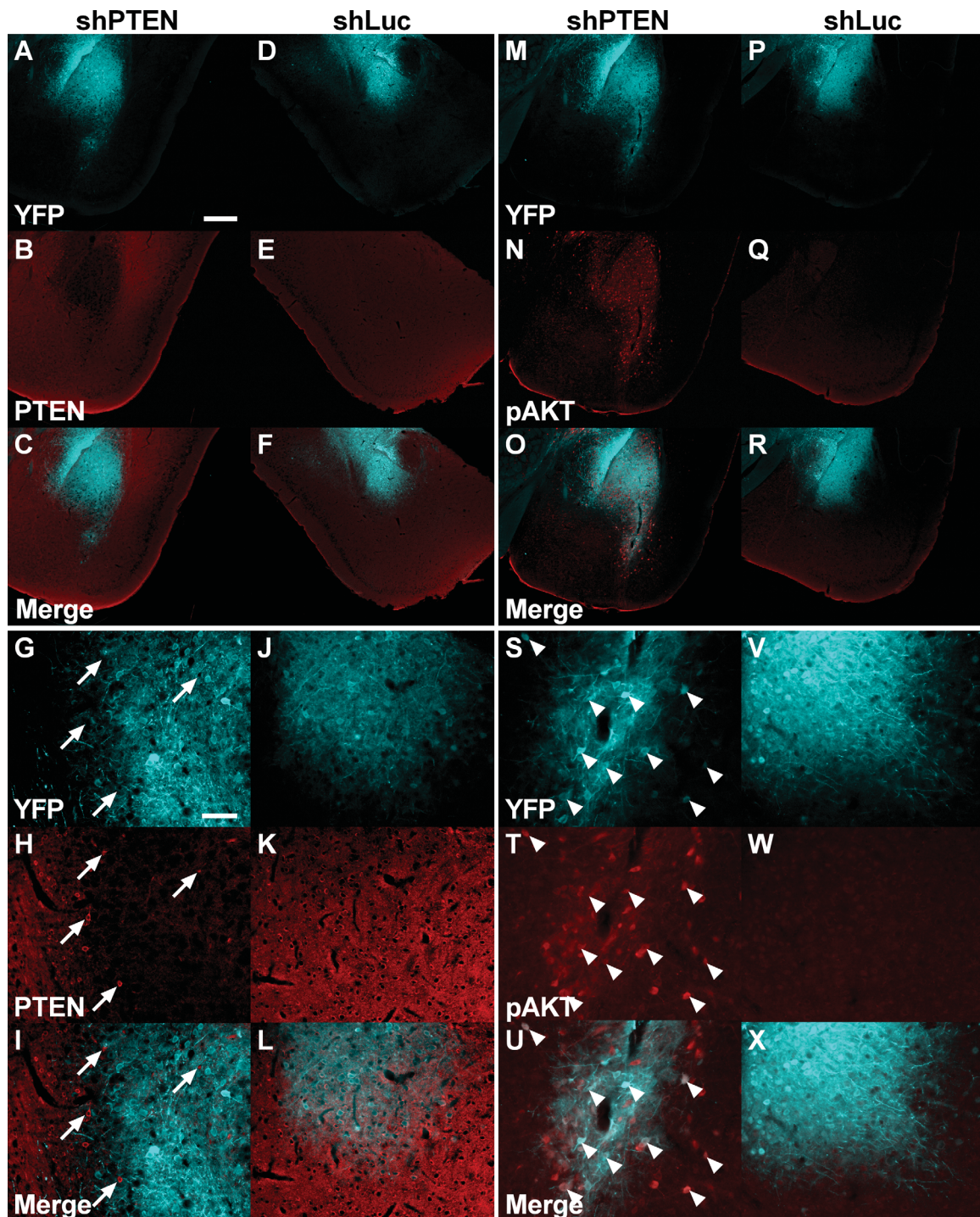


Figure 2. shPTEN-infected cells experience a robust decrease in PTEN expression and a resultant increase in phosphorylated AKT. **A–L:** Double immunofluorescent staining of YFP (cyan) PTEN (red). shPTEN-infected cells exhibit a dramatic decrease in PTEN expression levels (A–C low power; G–I high power), whereas shLuc-infected cells do not decrease PTEN expression (D–F low power; J–L high power). Arrows point to cells within or at the borders of the infected region that still express PTEN and are not YFP positive. **M–X:** Double immunofluorescent staining of YFP (cyan) and phosphorylated AKT (pAKT, red). shPTEN-infected cells display upregulated levels of pAKT (M–O low power; S–U high power), whereas shLuc-infected cells do not express significant levels of pAKT (P–R low power; V–X high power). Arrowheads point to individual cells that are double positive for YFP and pAKT. Scale bar = 500 μ m in A (applies to A–F, M–R; 100 μ m in G (applies to G–L, S–X).

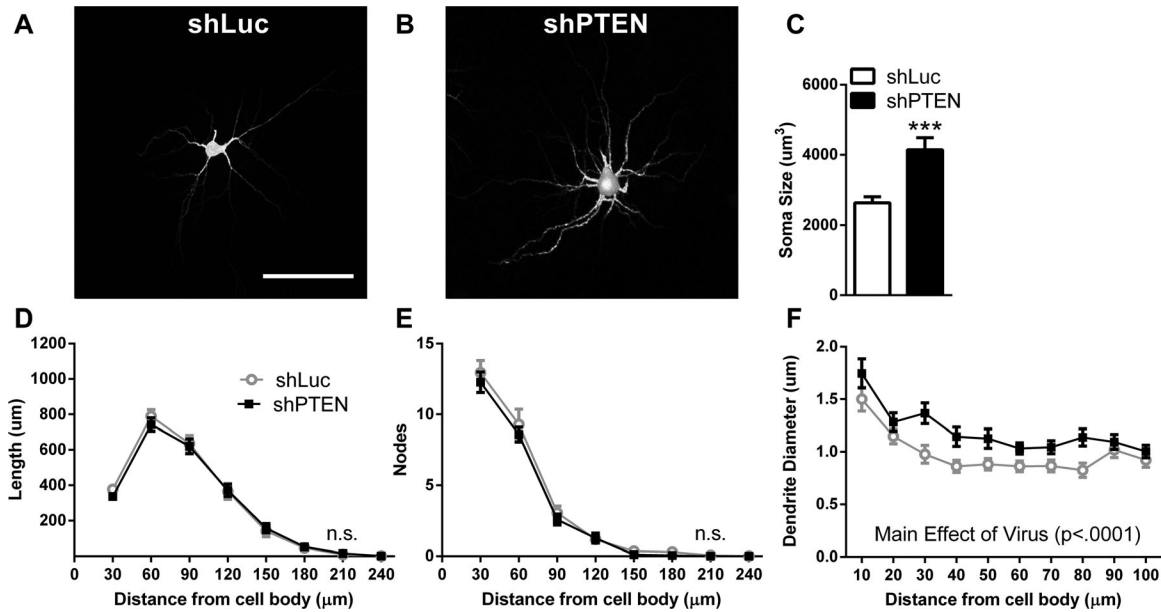


Figure 3. Soma size and dendrite width are increased in shPTEN-infected cells compared with shLuc-infected cells in the BLA. **A,B:** Representative images of shLuc (A) and shPTEN (B) infected neurons filled with the red Fluor 568 fluorescent dye. **C:** Quantification of 3D soma size (μm^3) was analyzed after 3D reconstruction of neurons using NeuroLucida. **D,E:** A Scholl analysis was performed on 3D reconstructions of Alexa Fluor 568-filled neurons by using concentric circles whose radii increased incrementally by 30 μm . There was no difference in length of dendrites (D) or intersections of dendrites with concentric circles (E). **F:** Dendrite diameter was measured in 10- μm increments. One dendritic segment was pseudo-randomly chosen and measured for each neuron at each distance. ($n = 17$ shLuc-infected neurons and $n = 16$ shPTEN-infected neurons.) *** $P < 0.001$; n.s., not significant. Scale bar = 100 μm in A (applies to A,B).

expressing viral YFP, whereas shLuc-infected tissue (Fig. 2D–F) showed no change in PTEN levels in regions expressing viral YFP. When these sections were imaged with higher magnification, cells located within or bordering the shPTEN-infected region that expressed detectable levels of PTEN did not express YFP (Fig. 2G–I). However, in the shLuc-infected cells, no detectable change in PTEN levels was observed among cells inside or outside the infected region (Fig. 2J–L). Thus, shPTEN effectively reduced PTEN levels, whereas the control virus, shLuc, did not.

To determine whether PTEN function also decreased after shPTEN viral infection, we assessed the expression of phosphorylated AKT (pAKT), which is downstream of PTEN and PI3K. Under normal conditions PTEN functions to decrease the amount of phosphatidylinositol trisphosphate, thereby decreasing PI3K activity and decreasing pAKT in the cell. Thus, with decreased PTEN function we expected increased pAKT within the shPTEN-infected region. When we colocalized the virally expressed YFP and pAKT, low-magnification images revealed that shPTEN infection dramatically increased pAKT levels (Fig. 2M–O), whereas shLuc-infected tissue displayed no increase in pAKT levels (Fig. P–R). Under higher magnification we observed that cells infected with the shPTEN virus had increased

pAKT levels (Fig. 2S–U), whereas shLuc-infected cells did not (Fig. 2V–X). Both the PTEN and pAKT immunohistochemistry experiments were repeated in three pairs of mice infected with shPTEN or shLuc with representative images shown in Figure 2.

PTEN knockdown in BLA neurons induces neuronal hypertrophy

To measure changes in the morphology of virally infected neurons, YFP+ BLA neurons were loaded with the red fluorescent dye Alexa Fluor 568. Z-stack images of loaded cells (Fig. 3A,B) were used to digitally reconstruct infected cells and analyze soma size, dendritic length, and dendritic branching. Somas of shPTEN-infected neurons were found to be significantly larger than in shLuc-infected neurons (Fig. 3C; shPTEN, $4,143.0 \pm 345.9 \mu\text{m}^3$; shLuc, $2,636.1 \pm 176.3 \mu\text{m}^3$; $n = 18$, $P < 0.001$ using Student's *t*-test). When we performed a Scholl analysis by using concentric circles whose radii increase in increments of 30 μm , we found no change in total dendritic length (data not shown) or in the length of dendrite at any specific distance from the cell body between shPTEN- and shLuc-infected neurons (Fig. 3D). We also did not detect any change in the total number of branch points (data not shown) or

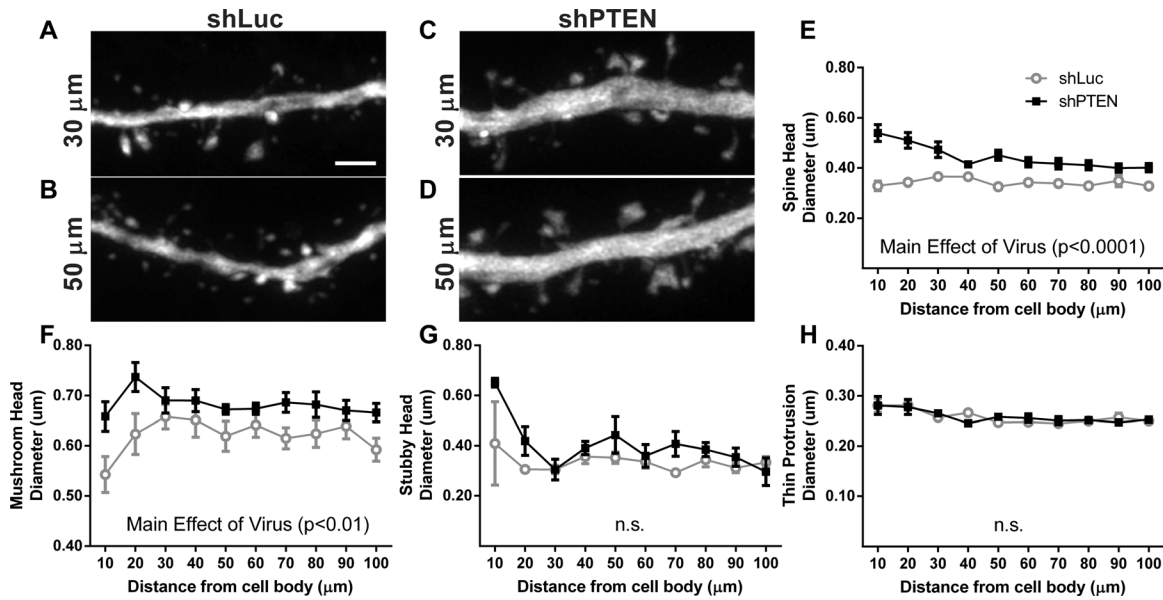


Figure 4. Mushroom spine head diameter is significantly increased in the shPTEN-infected neurons. **A–D:** Representative images of Alexa Fluor 568–filled dendritic segments from shLuc-infected (A,B) and shPTEN-infected (C,D) neurons at 30 μm and 50 μm away from the cell body. **E:** Average spine head diameter is increased in shPTEN-infected neurons compared with shLuc-infected neurons. **F–H:** A detailed analysis of spine subtypes reveals that this increased spine head diameter is due to an increase in mushroom spine head diameter (F) whereas stubby spines (G) and thin protrusions (H) show no increase in spine head diameter. ($n = 17$ shLuc-infected neurons and $n = 16$ shPTEN-infected neurons.) n.s., not significant. Scale bar = 2.5 μm in A (applies to A–D).

number of branch points (nodes) at any specific distance from the cell body between the two groups (Fig. 3E). We did observe, however, a dramatic increase in dendrite diameter of shPTEN-infected neurons that seemed to be most prominent from 30 to 80 μm from the cell body (Fig. 3F; two-way ANOVA; main effect of virus, $F_{(1,310)} = 35.02$, $P < 0.0001$; main effect of distance, $F_{(9,310)} = 13.58$, $P < 0.0001$; virus \times distance interaction, $F_{(9,310)} = 0.81$, $P = 0.61$). This difference in dendrite diameter between shLuc- and shPTEN-infected neurons is also illustrated in Figure 4A–D. The increase in dendritic caliber and soma size are consistent with what is known about the knockdown and knockout of PTEN in the DG (Kwon et al., 2003, 2006; Luikart et al., 2011; Zhou et al., 2009).

PTEN knockdown causes a decrease in thin protrusion density at distal dendritic segments and a global increase in mushroom spine size and density

Cell body and dendrite diameters were increased in the shPTEN neurons, and we wondered whether spine head diameter might also be increased. Thus, we analyzed spine heads and identified a significant increase in spine head diameter in PTEN knockdown neurons compared with shLuc-infected control neurons. Spine

head diameter was measured by using confocal microscopy to take high-magnification, high-resolution, z-stack images of dendritic segments every 10 μm up to 100 μm from the cell body (Fig. 4A–D shows representative images). Overall, average spine head diameter was increased in shPTEN neurons compared with shLuc neurons at all dendritic distances measured (Fig. 4E; two-way ANOVA; main effect of virus, $F_{(1,26)} = 25.14$, $P < 0.0001$; main effect of distance, $F_{(9,234)} = 2.58$, $P < 0.01$; virus \times distance interaction, $F_{(9,234)} = 10.54$, $P < 0.0001$).

In addition to determining the overall spine head diameter, which could be affected simply by increasing the proportion of mushroom-shaped spines compared with thin protrusions, we subcategorized spines/protrusions into mushroom spines, stubby spines, and thin protrusions. We then observed that mushroom spine head diameter as a separate group was increased in the shPTEN neurons (Fig. 4F; main effect of virus $F_{(1,17)} = 9.14$, $P < 0.01$; main effect of distance, $F_{(9,153)} = 2.19$; $P < 0.05$; virus \times distance interaction, $F_{(9,153)} = 1.35$, $P = 0.21$). Stubby spine and thin protrusion head diameters, however, were not different between shLuc and shPTEN neurons (Fig. 4G and H, respectively; thin protrusion “head diameters” were equated with distal neck diameters when no clear head was identified). Thus, it appears that the overall

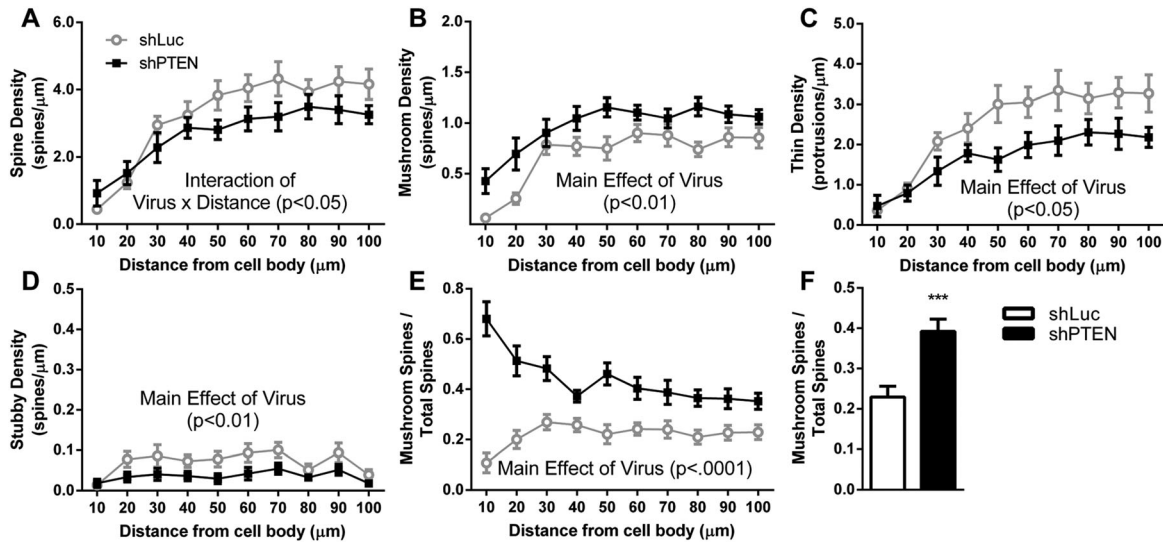


Figure 5. Fraction of mushroom spines is increased in shPTEN-infected cells. **A:** Spine density is decreased in more distal dendrite segments. **B–D:** An analysis of spine subtypes reveals that although thin protrusions (C) and stubby spines (D) account for the decrease in total spine density, mushroom spine density (B) is significantly increased. **E:** There is a significant shift toward an increased fraction of mushroom spine density, particularly in the more proximal dendrite segments. **F:** The total mushroom spine density fraction including all distances from the cell body is increased in the shPTEN-infected neurons compared with controls. ($n = 17$ shLuc-infected neurons and $n = 16$ shPTEN-infected neurons; **** $P < 0.0001$).

increase in spine head diameter of shPTEN neurons in the BLA can be attributed to the increase in mushroom spine head diameter in addition to possible changes in the proportion of mushroom spines.

Because knocking down PTEN has been reported by us and others to increase spine density (Kwon et al., 2006; Luikart et al., 2011; Zhou et al., 2009), we also measured spine density in shPTEN and shLuc neurons. Contrary to our own and others' previous findings using less sensitive measures, we did not find an increase in total spine density; on the contrary, statistical analysis revealed an interaction between virus and distance that suggested a *decrease* in total spine density in shPTEN neurons at the more distal segments compared with shLuc neurons with no change in density more proximally. (Fig. 5A; two-way rmANOVA; main effect of virus, $F_{(1,31)} = 2.13$, $P = 0.15$; main effect of distance, $F_{(9,279)} = 32.72$, $P < 0.0001$; virus \times distance interaction, $F_{(9,279)} = 2.02$, $P < 0.05$).

To tease apart the contribution of different spine types to spine density, we evaluated the density of mushroom spines, stubby spines, and thin protrusions independently. This analysis demonstrated that mushroom spine density was *increased* in shPTEN neurons compared with shLuc neurons, whereas both thin protrusion and stubby spine densities were *decreased* in shPTEN neurons compared with shLuc neurons (Fig. 5B–D; mushroom, main effect of virus $F_{(1,31)} = 10.96$,

$P < 0.01$; main effect of distance, $F_{(9,279)} = 19.70$, $P < 0.0001$; virus \times distance interaction $F_{(9,279)} = 1.02$, $P = 0.42$; thin, main effect of virus, $F_{(1,31)} = 5.12$, $P < 0.05$; main effect of distance, $F_{(9,279)} = 25.62$, $P < 0.0001$; virus \times distance interaction, $F_{(9,279)} = 2.07$, $P < 0.05$; stubby, main effect of virus, $F_{(1,31)} = 14.99$, $P < 0.001$; main effect of distance, $F_{(9,279)} = 2.97$, $P < 0.01$; virus \times distance interaction, $F_{(9,279)} = 0.61$, $P = 0.79$). These differential changes in spine/protrusion subtypes resulted in shPTEN neurons with a dramatically increased mushroom spine fraction along the entire length of the dendrite compared with shLuc neurons (Fig. 5E; main effect of virus, $F_{(1,26)} = 34.44$, $P < 0.0001$, main effect of distance, $F_{(9,234)} = 2.65$, $P < 0.01$; virus \times distance interaction, $F_{(9,234)} = 9.90$, $P < 0.0001$). When the mushroom spine fraction was calculated for the entire 100- μ m length of the dendrite, $39.2 \pm 3.02\%$ of spines in shPTEN neurons were mushroom spines, whereas only $22.95 \pm 2.64\%$ of spines were mushroom spines in shLuc neurons (Fig. 5F; Student's t -test, $P < 0.001$).

PTEN knockdown-induced shift from thin protrusions to mushroom spines is not specific to amygdala neurons

Our findings in basolateral amygdala neurons of decreased spine density at distal segments and a shift

from thin protrusions to mushroom spines directly contrasted with our own previous reports of increased spine density in DG granule neurons of PTEN conditional knockout mice. These findings could be explained by regional and neuronal differences or by an increased sensitivity of Alexa Fluor 568 cell filling followed by confocal spine imaging compared with previously used methods. In an effort to distinguish between these interpretations, we used the same fluorescent cell filling, imaging, and spine analysis techniques on DG granule neurons in PTEN conditional knockout mice (PTEN cKO) as we used in the BLA. We purposely used PTEN cKO mice rather than PTEN shRNA viral infection in the DG so that we could directly compare our fluorescent imaging results with our previous results from Golgi staining methods used in our prior publications (Kwon et al., 2006; Zhou et al., 2009). Similar to previous work in these PTEN cKO mice, images were taken of DG granule neuron dendrites spanning the 20–50- μm distance from the DG cell body layer (representative images in Fig. 6A,B).

As expected, and similar to our findings in the BLA and previous reports (Luikart et al., 2011; Zhou et al., 2009), we found that PTEN cKO neurons had increased dendrite diameter (Fig. 6C; WT, $0.80 \pm 0.04 \mu\text{m}$; PTEN cKO, $1.85 \pm 0.13 \mu\text{m}$, Student's *t*-test $P < 0.0001$). We also found that, similar to the BLA shPTEN neurons, spine head diameter was increased; in the DG, however, a significant increase in spine head diameter was observed across all three spine types including thin protrusions (Fig. 6D; All spines, WT $0.38 \pm 0.01 \mu\text{m}$, PTEN cKO $0.63 \pm 0.02 \mu\text{m}$, $P < 0.0001$; mushroom spines, WT $0.77 \pm 0.02 \mu\text{m}$, PTEN cKO $0.95 \pm 0.02 \mu\text{m}$, $P < 0.0001$; thin protrusions, WT $0.32 \pm 0.006 \mu\text{m}$, PTEN cKO $0.37 \pm 0.006 \mu\text{m}$, $P < 0.05$; stubby spines, WT $0.40 \pm 0.04 \mu\text{m}$, PTEN cKO $0.70 \pm 0.04 \mu\text{m}$, $P < 0.0001$).

As spine density was previously reported to be increased in DG granule neurons of PTEN cKO mice (Kwon et al., 2006), we expected similar results. However, we found that similar to the shPTEN neurons in the BLA, there was an increase in mushroom spine density with a corresponding decrease in thin protrusion density and a small increase in stubby spine density that resulted in no change in overall spine/protrusion density (Fig. 6E; all spines, WT 3.93 ± 0.27 spines/ μm , PTEN cKO 3.87 ± 0.33 spines/ μm , $P = 0.89$; mushroom spines, WT 0.48 ± 0.04 spines/ μm , PTEN cKO 1.67 ± 0.17 spines/ μm , $P < 0.0001$; thin protrusions, WT 3.36 ± 0.27 spines/ μm , PTEN cKO 2.02 ± 0.19 spines/ μm , $P < 0.001$; stubby, WT 0.09 ± 0.02 spines/ μm , PTEN cKO 0.18 ± 0.02 spines/ μm , $P < 0.01$). Finally, again similar to shPTEN neurons in the BLA, the

mushroom spine fraction (no. of mushroom spines/no. of total spines) in the PTEN cKO dentate granule neurons was significantly and dramatically increased compared with WT neurons (Fig. 6F; WT $12.9.0 \pm 1.2\%$, PTEN cKO $42.3 \pm 3.2\%$, $P < 0.0001$). Thus, PTEN deficiency-induced increases in mushroom spine density and corresponding decreases in thin protrusion density are common to both amygdala neurons and dentate granule neurons, even using different knockdown approaches and different durations of knockdowns. These results suggest a widespread role for the PTEN/PI3K/AKT/mTOR pathway in maintaining the proper balance of thin and mushroom spines in neurons in both brain regions.

shPTEN-infected neurons display increased miniature EPSC neurotransmission

Dendritic spines are a major site for excitatory synaptic neurotransmission (Bourne and Harris 2007). Spines of diverse sizes and morphologies are thought to represent different stages of spine maturity and to vary in function (Bourne and Harris, 2007; Matsuo et al., 2008). As demonstrated above, shPTEN-infected neurons had increased mushroom spine density, decreased thin protrusion density at distal segments, and increased spine head diameter. The differences in these dendritic spine parameters suggest that synaptic transmission may also be altered due to knockdown of PTEN. As an initial step in investigating this possibility, we recorded mEPSCs from the BLA in coronal brain slices 3–5 weeks after vector injection. shPTEN- or shLuc-infected neurons expressing YFP were detected by epifluorescence. We found that shPTEN-infected neurons showed a significant increase in mEPSC frequency (Fig. 7A,B; WT 1.18 ± 0.40 Hz, PTEN cKO 3.66 ± 1.01 Hz, $P < 0.030$). The amplitude of mEPSC was also increased (Fig. 7C,D; WT 17.39 ± 1.03 Hz, PTEN cKO $23.22 \pm 2.6\text{Hz}$, $P < 0.046$). Similar functional results have been published for dentate granule neurons with decreased PTEN (Luikart et al., 2011), supporting a conclusion of altered synaptic function due to PTEN knockdown.

Lack of associated behavioral abnormalities following PTEN knockdown in a subset of BLA neurons

Given previously published findings correlating increased BDNF expression and increased functional spine density in the BLA with increased anxiety-like behaviors (Govindarajan et al., 2006), we sought to determine whether decreased PTEN expression and resulting increased PI3K/AKT/mTOR signaling would

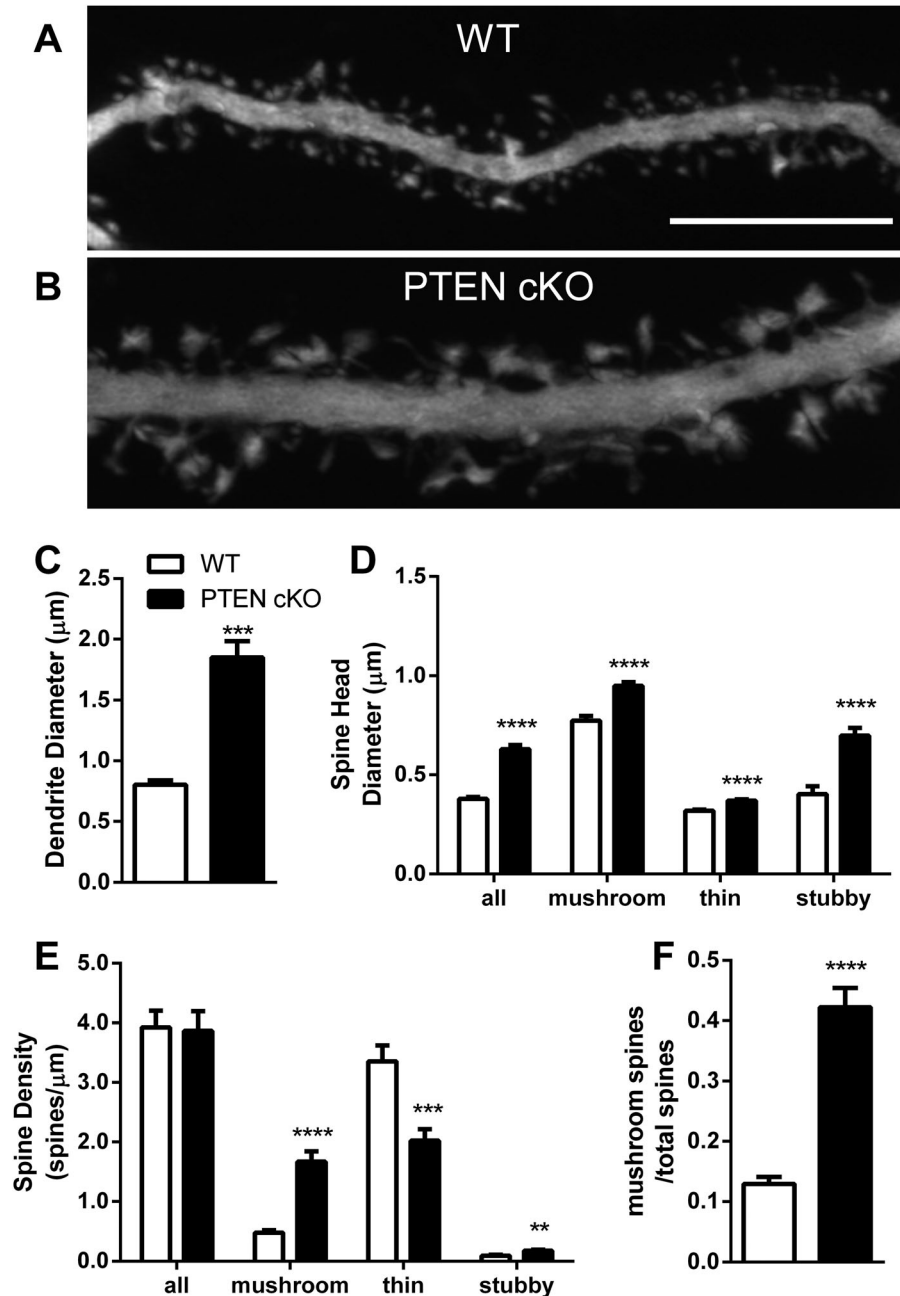


Figure 6. Dentate gyrus granule neurons in conditional PTEN KO mice have increased mushroom spine head diameter and an increase in the mushroom spine fraction with no change in total spine density. **A,B:** Representative images of Lucifer Yellow-filled WT (A) and PTEN-cKO (B) dentate gyrus granule neuron dendritic segments taken 20–50 μm from the dentate gyrus cell body layer. **C:** Diameter of the dendritic segments used for spine analysis. **D:** Average spine head diameter of all spine types, mushroom spines, thin protrusions, and stubby spines. **E:** Spine density of all spine types, mushroom spines, thin protrusions, and stubby spines. **F:** Quantification of the mushroom spine fraction. ($n = 17$ for both WT and PTEN-cKO neurons; $^{*}P < 0.01$; $^{***}P < 0.001$; $^{****}P < 0.0001$.) Scale bar = 10 μm in A (applies to A,B).

also correlate with increased anxiety-related behavior. In spite of a reduction in PTEN as demonstrated by immunohistochemistry and alterations in the number of functional, mature synaptic spines in the BLA, we observed no alterations in anxiety-related tasks including elevated

plus maze, open field, and dark/light box (Fig. 8A–C). Similarly, no alterations in other behavioral tasks were observed including social interaction with a juvenile, fear conditioning, startle threshold, social interaction in an open field, and locomotor activity (Fig. 8D–H).

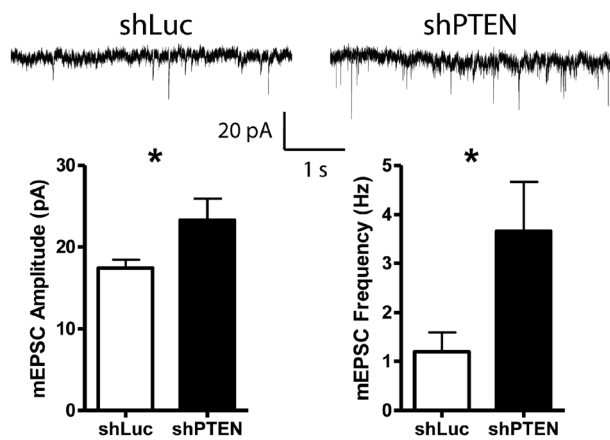


Figure 7. shPTEN-infected neurons show increased miniature EPSC amplitude and frequency. **Top:** Representative traces from shLuc and shPTEN mEPSC recordings. **Bottom Left:** Increased amplitude of mEPSCs in shPTEN compared with shLuc-infected BLA neurons. **Bottom Right:** Increased mEPSC frequency in shPTEN compared with shLuc-infected BLA neurons. (* $P < 0.05$; $n = 11$ shLuc and $n = 10$ shPTEN.)

DISCUSSION

Previous work by our laboratory and others reported that loss of PTEN from DG granule neurons causes neuronal hypertrophy and increased spine density (Kwon et al., 2001, 2006; Luikart et al., 2011). Loss of PTEN induces upregulation of pAKT and its downstream targets including mTOR. Inhibiting mTOR reversed the neuronal and synaptic effects of PTEN deletion in DG granule neurons (Kwon et al., 2003; Zhou et al., 2009). Additionally, PTEN knockdown increases mEPSC frequency and amplitude in DG granule neurons (Luikart et al., 2011). In accordance with these reports, we found neuronal hypertrophy in BLA neurons after virally mediated PTEN knockdown, measured as increased soma size and dendritic caliber (Fig. 3C,F). Thus, many of our findings support and extend previous work on PTEN in the brain. Moreover, we extended previous findings to include increased diameter of mushroom spine heads (Figs. 4F,G & 6D).

In contrast to previous reports, however, our data suggest that PTEN knockdown in neurons does not increase total spine/protrusion density, but instead induces a shift in the mushroom/thin ratio such that the density of mushroom spines is increased whereas thin protrusion density is decreased in distal dendritic segments (Fig. 5). In our analysis of spine morphology, we are unable to distinguish between thin spines and filopodia, leaving room to question whether one or both of those categories of protrusions is decreasing after PTEN knockdown. Nevertheless, our findings are strengthened by similar results in a second brain region

using cre recombination for PTEN knockdown and imaging spines in older mice (6 months old). In addition, our results following relatively acute viral knockdown in the BLA and those following chronic knockout of PTEN in the DG demonstrate similar effects.

Interestingly, we still observed an increase in spontaneous synaptic activity in shPTEN-infected BLA neurons in spite of a decrease in total spine density at more distal segments (Fig. 7). The increased mEPSC frequency is most parsimoniously explained by increased density of mushroom spines, thought to represent more mature/active synapses (Bourne and Harris, 2007), relative to thin protrusion density. Of course, mEPSC recordings favor synapses that are electrotonically closer to the soma. Our data suggest that upregulation of the PI3K/AKT/mTOR pathway does not increase spine/protrusion density, but instead increases the fraction of more mature, functional synapses in the BLA.

Because most studies examining the effects of PTEN knockdown on spine density were done in the DG (Kwon et al., 2001, 2006; Luikart et al., 2011), one explanation for our novel findings in the BLA could be that the DG and BLA respond differently to PTEN knockdown. However, our findings were similar in both brain regions. Alternatively, our results could be explained by a difference in spine imaging technique. Previous studies used Golgi staining and light microscopy (Govindarajan et al., 2006; Kwon et al., 2006) or confocal imaging of virally expressed GFP (Luikart et al., 2011). Virally expressed GFP may not be concentrated enough in small spines for their detection, or there may be significant background signal due to many cells expressing GFP. In addition, imaging spines after Golgi staining prevents the observation of spines in front of or behind the dendrite, yielding an apparently lower total spine density. Cell filling, however, may allow for an improved, 3D resolution due to a high intensity of fluorescent dye in spines and throughout the dendrites while producing little to no background from surrounding tissue or cells. We postulate that these differences in resolution resulted in better detection of thin protrusions and smaller spines in our study as a result of more efficient spread of fluorescent dyes into even the thinnest dendritic protrusions. Another potential explanation for our different findings may simply be differences in fixation techniques and artifacts that could have been induced by our methods. Such artifactual differences, of course, would have to be differentially affected by the status of PTEN knockdown because we see clear, significant differences between control and experimental conditions in spine density.

To examine these alternative explanations for our novel findings, we measured spine density in DG

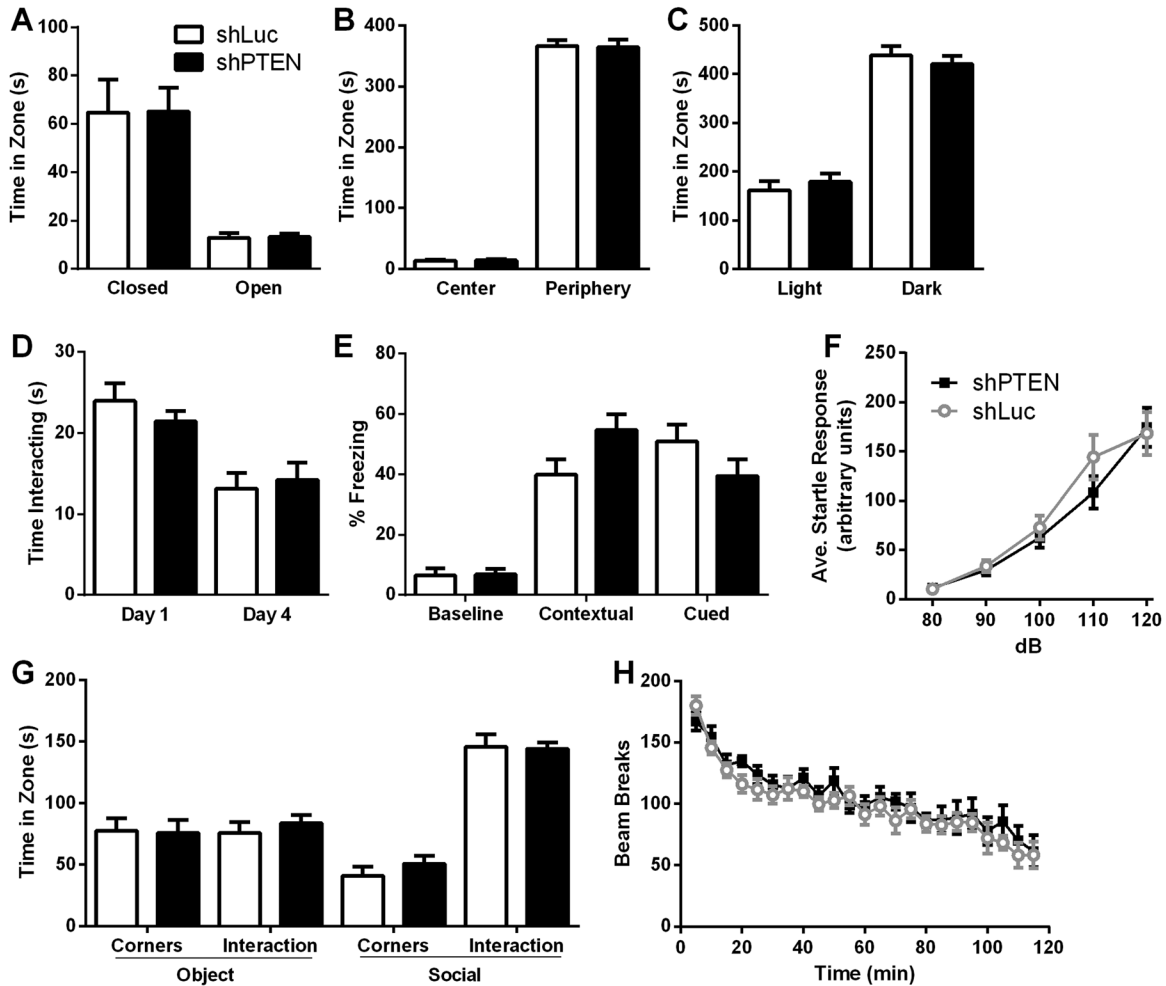


Figure 8. shPTEN-injected mice do not show behavioral phenotypes 3 weeks post injection. **A–C:** No difference was observed between shPTEN- and shLuc-injected mice in three tests of anxiety: elevated plus maze (A), open field (B), and dark/light box (C). **D–H:** Additionally, no differences were observed in social interaction with a juvenile (D), both contextual and cued fear conditioning (E), startle threshold (F), social interaction in the open field (G), and locomotion (H). ($n = 12$ shLuc mice and $n = 15$ shPTEN mice.)

granule neurons in PTEN cKO mice using the cell-fill approach. PTEN knockdown in the DG decreased thin protrusion density and increased mushroom spine density without changing total spine density (Fig. 6E,F). The similar results in the DG and BLA using two different approaches for knocking down PTEN, along with increased overall spine density counts using our technique compared with previous reports (Kwon et al., 2006; Luikart et al., 2011; Zhou et al., 2009), support the hypothesis that cell-filling techniques allow for better visualization of small spines and more accurate measurement of PTEN's effects on spine density/morphology. Overall, these data imply that loss of PTEN has similar effects on spine density and morphology in the DG and BLA neurons, and that in order to observe this shift from thin protrusions to mushroom spines one must be able to image the smaller thin protrusions that

may be missed with other techniques. It is of additional interest that both chronic PTEN deletion in the DG and more acute PTEN knockdown in the BLA led to qualitatively similar results.

Similar to studies in the hippocampus (Luikart et al., 2011), we demonstrate that knockdown of PTEN in the BLA causes an increase in the frequency and amplitude of mEPSCs. As pointed out above, although we saw no indication suggesting an increase in the total number of synapses after PTEN knockdown, there was an important increase in the relative number and size of mushroom spines all along the dendritic arborization. Mushroom spines are thought to be more active than thin protrusions (Fiala et al., 2002). Interestingly, spine head volume correlates with the size of the presynaptic readily releasable pool and with the number of docked vesicles (Dobrunz and Stevens, 1997; Harris and

Stevens, 1989), which could affect the frequency of mEPSCs due to presynaptic changes. Furthermore, the size of dendritic spines is also correlated with the area of the postsynaptic density and the number of glutamatergic receptors at the synapse (Arellano et al., 2007; Harris and Stevens, 1989; Nusser et al., 1998). This is consistent with the increase in mEPSC amplitude shown here after knockdown of PTEN. Increased mEPSC amplitude is also consistent with a similar outcome due to an increase in surface expression of AMPA receptors after leptin-induced PTEN inhibition (Moult et al., 2010). Thus, the increase in frequency and amplitude in mEPSCs observed after knockdown of PTEN in the BLA is correlated with an increase in the number and diameter of the “more mature” mushroom-type of synapse.

Because the amygdala is part of the circuitry known to regulate fear and anxiety (Davis et al., 1994; Johnson et al., 2008; LeDoux, 2007), we predicted that knockdown of PTEN and corresponding increases in synaptic spine size and function would alter related behaviors in our model. Despite BLA neuronal hypertrophy, shifting of spine subtypes, and increased mEPSC frequency and amplitude in neurons lacking PTEN expression in the BLA, these changes had no effect on multiple amygdala-dependent behaviors. Although these negative behavioral data are important to report, they do not exclude a role for PTEN in the BLA in any of the behavioral tasks reported due to the virus only targeting 60% of BLA neurons within infected regions. Indeed, PTEN and other factors downstream of BDNF may still be responsible for the increased anxiety-related behaviors observed in BDNF-overexpressing mice (Govindarajan et al., 2006). Alternative techniques of manipulating PTEN in the BLA may shed further light on the role of PTEN in behavior.

PTEN mutations have been implicated in human autism (Boccone et al., 2006; Butler et al., 2005; Buxbaum et al., 2007; Goffin et al., 2001; Herman et al., 2007; McBride et al., 2010; Orrico et al., 2009; Stein et al., 2010; Varga et al., 2009; Zori et al., 1998), and PTEN conditional knockout limited to the cortex and hippocampus results in alterations in social interaction, an effect that can be reversed by mTOR inhibition (Kwon et al., 2006; Zhou et al., 2009). In the present study, we assessed whether PTEN knockdown isolated to the BLA could result in social behavior abnormalities. Interestingly, we found no alterations in locomotor activity, social interaction with a juvenile, social interaction in an open field, startle threshold, fear conditioning, or footshock threshold in mice treated with shPTEN in the bilateral BLA. These findings support the conclusion that the social and anxiety phenotypes observed in the PTEN conditional KO mice (Kwon et al., 2006; Zhou

et al., 2009) are subserved largely by loss of PTEN in the hippocampus or cortex, the brain regions in which PTEN was conditionally deleted in this model. As noted, however, the present study does not completely rule out a role for PTEN in the BLA in any of the behaviors examined due to only a fraction of BLA neurons being affected.

In summary, our findings support a novel role for PTEN in modulation of spine morphology. Our data suggest that the mechanism leading to increased synaptic activity after PTEN knockdown may not be increased total spine density. Instead, our data implicate the PTEN/PI3K/AKT/mTOR pathway as an inducer of synaptic maturation by shifting the mushroom/thin ratio in favor of mushroom spines without dramatically altering total spine/protrusion density. It seems most likely that loss of PTEN results in conversion of thin protrusions into mature, functional mushroom spines. We cannot rule out, however, the possibility that this shift is occurring via *de novo* mushroom spine formation with concurrent pruning of the thin protrusion population. Given the disease processes for which the PTEN/AKT/mTOR pathway has been implicated, including autism (Butler et al., 2005; Buxbaum et al., 2007), understanding the role of this pathway in neuronal and synaptic growth and maturation is vital to understanding the pathophysiology of these disorders.

ACKNOWLEDGMENTS

We thank Dr. Patrick Hoff, Dr. John Morisson, and Dr. Dani Dumitriu at Mount Sinai for training in the techniques used for neuronal cell fills and analysis using NeuronStudio Software. Dr. Michael Cherry and Nathan A. Haws helped with statistical analysis.

CONFLICT OF INTEREST STATEMENT

The authors declare no competing financial interests.

ROLE OF AUTHORS

All authors had full access to all the data in the study and take responsibility for the integrity of the data and the accuracy of the data analysis. M.E.H. and C.M.P. conceived and designed the experiments; M.E.H., T.J., F.E-B., A.W., G.D.S., D.R.S., and G.S. carried them out with input from C.M.P., M.K., S.R., and A.B.; M.E.H., F.E-B., G.D.S., and C.M.P. performed statistical analysis; and M.E.H. wrote the paper with input from all authors.

LITERATURE CITED

Abel TW, Baker SJ, Fraser MM, Tihan T, Nelson JS, Yachnis AT, Bouffard JP, Mena H, Burger PC, Eberhart CG. 2005. Lhermitte-Duclos disease: a report of 31 cases with

- immunohistochemical analysis of the PTEN/AKT/mTOR pathway. *J Neuropathol Exp Neurol* 64:341–349.
- Arellano JI, Benavides-Piccione R, Defelipe J, Yuste R. 2007. Ultrastructure of dendritic spines: correlation between synaptic and spine morphologies. *Front Neurosci* 1:131–143.
- Backman SA, Stambolic V, Suzuki A, Haight J, Elia A, Pretorius J, Tsao MS, Shannon P, Bolon B, Ivy GO, Mak TW. 2001. Deletion of Pten in mouse brain causes seizures, ataxia and defects in soma size resembling Lhermitte-Duclos disease. *Nat Genet* 29:396–403.
- Bartlett JS, Samulski RJ, McCown TJ. 1998. Selective and rapid uptake of adeno-associated virus type 2 in brain. *Hum Gene Ther* 9:1181–1186.
- Besson A, Robbins SM, Yong VW. 1999. PTEN/MMAC1/TEP1 in signal transduction and tumorigenesis. *Eur J Biochem* 263:605–611.
- Blundell J, Tabuchi K, Bolliger MF, Blaiss CA, Brose N, Liu X, Sudhof TC, Powell CM. 2009. Increased anxiety-like behavior in mice lacking the inhibitory synapse cell adhesion molecule neuroligin 2. *Genes Brain Behav* 8:114–126.
- Blundell J, Kaeser PS, Sudhof TC, Powell CM. 2010. RIM1a-pha and interacting proteins involved in presynaptic plasticity mediate prepulse inhibition and additional behaviors linked to schizophrenia. *J Neurosci* 30:5326–5333.
- Boccone L, Dessi V, Zappu A, Piga S, Piludu MB, Rais M, Massidda C, De Virgiliis S, Cao A, Loudianos G. 2006. Bannayan-Riley-Ruvalcaba syndrome with reactive nodular lymphoid hyperplasia and autism and a PTEN mutation. *Am J Med Genet* 140:1965–1969.
- Bourne J, Harris KM. 2007. Do thin spines learn to be mushroom spines that remember? *Curr Opin Neurobiol* 17:381–386.
- Butler MG, Dasouki MJ, Zhou XP, Talebizadeh Z, Brown M, Takahashi TN, Miles JH, Wang CH, Stratton R, Pilarski R, Eng C. 2005. Subset of individuals with autism spectrum disorders and extreme macrocephaly associated with germline PTEN tumour suppressor gene mutations. *J Med Genet* 42:318–321.
- Buxbaum JD, Cai G, Chaste P, Nygren G, Goldsmith J, Reichert J, Anckarsater H, Rastam M, Smith CJ, Silverman JM, Hollander E, Leboyer M, Gillberg C, Verloes A, Betancur C. 2007. Mutation screening of the PTEN gene in patients with autism spectrum disorders and macrocephaly. *Am J Med Genet B Neuropsychiatr Genet* 144B:484–491.
- Dahia PL. 2000. PTEN, a unique tumor suppressor gene. *Endocr Relat Cancer* 7:115–129.
- Davis M, Rainnie D, Cassell M. 1994. Neurotransmission in the rat amygdala related to fear and anxiety. *Trends Neurosci* 17:208–214.
- Di Cristofano A, Pandolfi PP. 2000. The multiple roles of PTEN in tumor suppression. *Cell* 100:387–390.
- Dobrunz LE, Stevens CF. 1997. Heterogeneity of release probability, facilitation, and depletion at central synapses. *Neuron* 18:995–1008.
- Downes CP, Bennett D, McConnachie G, Leslie NR, Pass I, MacPhee C, Patel L, Gray A. 2001. Antagonism of PI 3-kinase-dependent signalling pathways by the tumour suppressor protein, PTEN. *Biochem Soc Trans* 29:846–851.
- Dumitriu D, Hao J, Hara Y, Kaufmann J, Janssen WG, Lou W, Rapp PR, Morrison JH. 2010. Selective changes in thin spine density and morphology in monkey prefrontal cortex correlate with aging-related cognitive impairment. *J Neurosci* 30:7507–7515.
- Dumitriu D, Rodriguez A, Morrison JH. 2011. High-throughput, detailed, cell-specific neuroanatomy of dendritic spines using microinjection and confocal microscopy. *Nat Protoc* 6:1391–1411.
- Dumitriu D, Berger SI, Hamo C, Hara Y, Bailey M, Hamo A, Grossman YS, Janssen WG, Morrison JH. 2012a. Vamping: stereology-based automated quantification of fluorescent puncta size and density. *J Neurosci Methods* 209:97–105.
- Dumitriu D, Laplant Q, Grossman YS, Dias C, Janssen WG, Russo SJ, Morrison JH, Nestler EJ. 2012b. Subregional, dendritic compartment, and spine subtype specificity in cocaine regulation of dendritic spines in the nucleus accumbens. *J Neurosci* 32:6957–6966.
- Encinas JM, Vahtokari A, Enikolopov G. 2006. Fluoxetine targets early progenitor cells in the adult brain. *Proc Natl Acad Sci U S A* 103:8233–8238.
- Eng C. 1999. The role of PTEN, a phosphatase gene, in inherited and sporadic nonmedullary thyroid tumors. *Recent Prog Horm Res* 54:441–452; discussion 453.
- Eng C. 2003. PTEN: one gene, many syndromes. *Hum Mutat* 22:183–198.
- Fiala JC, Allwardt B, Harris KM. 2002. Dendritic spines do not split during hippocampal LTP or maturation. *Nat Neurosci* 5:297–298.
- Forster MD, Dedes KJ, Sandhu S, Frentzas S, Kristeleit R, Ashworth A, Poole CJ, Weigelt B, Kaye SB, Molife LR. 2011. Treatment with olaparib in a patient with PTEN-deficient endometrioid endometrial cancer. *Nat Rev Clin Oncol* 8:302–306.
- Fraser MM, Bayazitov IT, Zakharenko SS, Baker SJ. 2008. Phosphatase and tensin homolog, deleted on chromosome 10 deficiency in brain causes defects in synaptic structure, transmission and plasticity, and myelination abnormalities. *Neuroscience* 151:476–488.
- Goffin A, Hoefsloot LH, Bosgoed E, Swillen A, Fryns JP. 2001. PTEN mutation in a family with Cowden syndrome and autism. *Am J Med Genet* 105:521–524.
- Govindarajan A, Rao BS, Nair D, Trinh M, Mawjee N, Tonegawa S, Chattarji S. 2006. Transgenic brain-derived neurotrophic factor expression causes both anxiogenic and antidepressant effects. *Proc Natl Acad Sci U S A* 103:13208–13213.
- Hao J, Rapp PR, Leffler AE, Leffler SR, Janssen WG, Lou W, McKay H, Roberts JA, Wearne SL, Hof PR, Morrison JH. 2006. Estrogen alters spine number and morphology in prefrontal cortex of aged female rhesus monkeys. *J Neurosci* 26:2571–2578.
- Harris KM, Stevens JK. 1989. Dendritic spines of CA 1 pyramidal cells in the rat hippocampus: serial electron microscopy with reference to their biophysical characteristics. *J Neurosci* 9:2982–2997.
- Herman GE, Butter E, Enrile B, Pastore M, Prior TW, Sommer A. 2007. Increasing knowledge of PTEN germline mutations: two additional patients with autism and macrocephaly. *Am J Med Genet* 143:589–593.
- Hobert JA, Eng C. 2009. PTEN hamartoma tumor syndrome: an overview. *Genet Med* 11:687–694.
- Hoeffler CA, Klann E. 2010. mTOR signaling: at the crossroads of plasticity, memory and disease. *Trends Neurosci* 33:67–75.
- Johnson LR, Hou M, Ponce-Alvarez A, Gribelyuk LM, Alphas HH, Albert L, Brown BL, Ledoux JE, Doyere V. 2008. A recurrent network in the lateral amygdala: a mechanism for coincidence detection. *Front Neural Circuits* 2:3.
- Kwon CH, Zhu X, Zhang J, Knoop LL, Tharp R, Smeyne RJ, Eberhart CG, Burger PC, Baker SJ. 2001. Pten regulates

- neuronal soma size: a mouse model of Lhermitte-Duclos disease. *Nat Genet* 29:404–411.
- Kwon CH, Zhu X, Zhang J, Baker SJ. 2003. mTor is required for hypertrophy of Pten-deficient neuronal soma in vivo. *Proc Natl Acad Sci U S A* 100:12923–12928.
- Kwon CH, Luikart BW, Powell CM, Zhou J, Matheny SA, Zhang W, Li Y, Baker SJ, Parada LF. 2006. Pten regulates neuronal arborization and social interaction in mice. *Neuron* 50:377–388.
- Lakshminarasimhan H, Chattarji S. 2012. Stress leads to contrasting effects on the levels of brain derived neurotrophic factor in the hippocampus and amygdala. *PLoS One* 7:e30481.
- LeDoux J. 2007. The amygdala. *Curr Biol* 17:R868–874.
- Leslie NR, Downes CP. 2002. PTEN: The down side of PI 3-kinase signalling. *Cell Signal* 14:285–295.
- Li J, Yen C, Liaw D, Podsypanina K, Bose S, Wang SI, Puc J, Miliareis C, Rodgers L, McCombie R, Bigner SH, Giovanella BC, Ittmann M, Tycko B, Hibshoosh H, Wigler MH, Parsons R. 1997. PTEN, a putative protein tyrosine phosphatase gene mutated in human brain, breast, and prostate cancer. *Science* 275:1943–1947.
- Luikart BW, Schnell E, Washburn EK, Bensen AL, Tovar KR, Westbrook GL. 2011. Pten knockdown in vivo increases excitatory drive onto dentate granule cells. *J Neurosci* 31:4345–4354.
- Maehama T, Dixon JE. 1998. The tumor suppressor, PTEN/MMAC1, dephosphorylates the lipid second messenger, phosphatidylinositol 3,4,5-trisphosphate. *J Biol Chem* 273:13375–13378.
- Maehama T, Dixon JE. 1999. PTEN: a tumour suppressor that functions as a phospholipid phosphatase. *Trends Cell Biol* 9:125–128.
- Matsuo N, Reijmers L, Mayford M. 2008. Spine-type-specific recruitment of newly synthesized AMPA receptors with learning. *Science* 319:1104–1107.
- McBride KL, Varga EA, Pastore MT, Prior TW, Manickam K, Atkin JF, Herman GE. 2010. Confirmation study of PTEN mutations among individuals with autism or developmental delays/mental retardation and macrocephaly. *Autism Res* 3:137–141.
- McDonald AJ. 1982. Neurons of the lateral and basolateral amygdaloid nuclei: a Golgi study in the rat. *J Comp Neurol* 212:293–312.
- McIlwain KL, Merriweather MY, Yuva-Paylor LA, Paylor R. 2001. The use of behavioral test batteries: effects of training history. *Physiol Behav* 73:705–717.
- Moldrich RX, Gobius I, Pollak T, Zhang J, Ren T, Brown L, Mori S, De Juan Romero C, Britanova O, Tarabykin V, Richards LJ. 2010. Molecular regulation of the developing commissural plate. *J Comp Neurol* 518:3645–3661.
- Moult PR, Cross A, Santos SD, Carvalho AL, Lindsay Y, Connolly CN, Irving AJ, Leslie NR, Harvey J. 2010. Leptin regulates AMPA receptor trafficking via PTEN inhibition. *J Neurosci* 30:4088–4101.
- Mullen RJ, Buck CR, Smith AM. 1992. NeuN, a neuronal specific nuclear protein in vertebrates. *Development* 116:201–211.
- Nelen MR, van Staveren WC, Peeters EA, Hassel MB, Gorlin RJ, Hamm H, Lindboe CF, Fryns JP, Sijmons RH, Woods DG, Mariman EC, Padberg GW, Kremer H. 1997. Germline mutations in the PTEN/MMAC1 gene in patients with Cowden disease. *Hum Mol Genet* 6:1383–1387.
- Nusser Z, Lujan R, Laube G, Roberts JD, Molnar E, Somogyi P. 1998. Cell type and pathway dependence of synaptic AMPA receptor number and variability in the hippocampus. *Neuron* 21:545–559.
- Orloff MS, Eng C. 2008. Genetic and phenotypic heterogeneity in the PTEN hamartoma tumour syndrome. *Oncogene* 27:5387–5397.
- Orrico A, Galli L, Buoni S, Orsi A, Vonella G, Sorrentino V. 2009. Novel PTEN mutations in neurodevelopmental disorders and macrocephaly. *Clin Genet* 75:195–198.
- Paylor R, Spencer CM, Yuva-Paylor LA, Pieke-Dahl S. 2006. The use of behavioral test batteries, II: effect of test interval. *Physiol Behav* 87:95–102.
- Powell CM, Schoch S, Monteggia L, Barrot M, Matos MF, Feldmann N, Sudhof TC, Nestler EJ. 2004. The presynaptic active zone protein RIM1alpha is critical for normal learning and memory. *Neuron* 42:143–153.
- Pun RY, Rolle IJ, Lasarge CL, Hosford BE, Rosen JM, Uhl JD, Schmeltzer SN, Faulkner C, Bronson SL, Murphy BL, Richards DA, Holland KD, Danzer SC. 2012. Excessive activation of mTOR in postnatally generated granule cells is sufficient to cause epilepsy. *Neuron* 75:1022–1034.
- Rodríguez A, Ehlenberger DB, Hof PR, Wearne SL. 2006. Rayburst sampling, an algorithm for automated three-dimensional shape analysis from laser scanning microscopy images. *Nat Protoc* 1:2152–2161.
- Rodríguez A, Ehlenberger DB, Dickstein DL, Hof PR, Wearne SL. 2008. Automated three-dimensional detection and shape classification of dendritic spines from fluorescence microscopy images. *PLoS One* 3:e1997.
- Steck PA, Pershouse MA, Jasser SA, Yung WK, Lin H, Ligon AH, Langford LA, Baumgard ML, Hattier T, Davis T, Frye C, Hu R, Swedlund B, Teng DH, Tavtigian SV. 1997. Identification of a candidate tumour suppressor gene, MMAC1, at chromosome 10q23.3 that is mutated in multiple advanced cancers. *Nat Genet* 15:356–362.
- Stein MT, Elias ER, Saenz M, Pickler L, Reynolds A. 2010. Autistic spectrum disorder in a 9-year-old girl with macrocephaly. *J Dev Behav Pediatr* 31:632–634.
- Stuber GD, Sparta DR, Stamatakis AM, van Leeuwen WA, Hardjoprajitno JE, Cho S, Tye KM, Kempadoo KA, Zhang F, Deisseroth K, Bonci A. 2011. Excitatory transmission from the amygdala to nucleus accumbens facilitates reward seeking. *Nature* 475:377–380.
- Suzuki A, Yamaguchi MT, Ohteki T, Sasaki T, Kaisho T, Kimura Y, Yoshida R, Wakeham A, Higuchi T, Fukumoto M, Tsubata T, Ohashi PS, Koyasu S, Penninger JM, Nakano T, Mak TW. 2001. T cell-specific loss of Pten leads to defects in central and peripheral tolerance. *Immunity* 14:523–534.
- Tabuchi K, Blundell J, Etherton MR, Hammer RE, Liu X, Powell CM, Sudhof TC. 2007. A neuroligin-3 mutation implicated in autism increases inhibitory synaptic transmission in mice. *Science* 318:71–76.
- Varga EA, Pastore M, Prior T, Herman GE, McBride KL. 2009. The prevalence of PTEN mutations in a clinical pediatric cohort with autism spectrum disorders, developmental delay, and macrocephaly. *Genet Med* 11:111–117.
- Vazquez F, Sellers WR. 2000. The PTEN tumor suppressor protein: an antagonist of phosphoinositide 3-kinase signaling. *Biochim Biophys Acta* 1470:M21–35.
- Waite KA, Eng C. 2002. Protean PTEN: form and function. *Am J Hum Genet* 70:829–844.
- Wearne SL, Rodríguez A, Ehlenberger DB, Rocher AB, Henderson SC, Hof PR. 2005. New techniques for imaging, digitization and analysis of three-dimensional neural morphology on multiple scales. *Neuroscience* 136:661–680.
- Xiong Q, Oviedo HV, Trotman LC, Zador AM. 2012. PTEN Regulation of local and long-range connections in mouse auditory cortex. *J Neurosci* 32:1643–1652.

Zhang XC, Piccini A, Myers MP, Van Aelst L, Tonks NK. 2012. Functional analysis of the protein phosphatase activity of PTEN. *Biochem J* 444:457–464.

Zhou J, Blundell J, Ogawa S, Kwon CH, Zhang W, Sinton C, Powell CM, Parada LF. 2009. Pharmacological inhibition of mTORC1 suppresses anatomical, cellular, and behav-

ioral abnormalities in neural-specific Pten knock-out mice. *J Neurosci* 29:1773–1783.

Zori RT, Marsh DJ, Graham GE, Marliss EB, Eng C. 1998. Germline PTEN mutation in a family with Cowden syndrome and Bannayan-Riley-Ruvalcaba syndrome. *Am J Med Genet* 80:399–402.